



ELSEVIER

Contents lists available at ScienceDirect

## Journal of Membrane Science

journal homepage: [www.elsevier.com/locate/memsci](http://www.elsevier.com/locate/memsci)

# Organosilane-functionalized graphene oxide for enhanced antifouling and mechanical properties of polyvinylidene fluoride ultrafiltration membranes



Zhiwei Xu<sup>a,\*</sup>, Jiguo Zhang<sup>a</sup>, Mingjing Shan<sup>a</sup>, Yinglin Li<sup>a</sup>, Baodong Li<sup>a</sup>, Jiarong Niu<sup>b</sup>,  
Baoming Zhou<sup>b</sup>, Xiaoming Qian<sup>b,\*\*</sup>

<sup>a</sup> State Key Laboratory of Hollow Fiber Membrane Materials and Processes, Tianjin Polytechnic University, Tianjin 300387, People's Republic of China

<sup>b</sup> School of Textiles, Tianjin Polytechnic University, Tianjin 300387, People's Republic of China

## ARTICLE INFO

## Article history:

Received 19 November 2013

Received in revised form

17 January 2014

Accepted 21 January 2014

Available online 4 February 2014

## Keywords:

Hybrid membranes

Graphene oxide

Graphene oxide functionalization

Antifouling performance

Mechanical performance

## ABSTRACT

Functionalized graphene oxide (f-GO) was synthesized by a simple covalent functionalization with 3-aminopropyltriethoxysilane (APTS). The hybrid polyvinylidene fluoride (PVDF) ultrafiltration membranes were then prepared by adding different ratios of graphene oxide (GO) and f-GO via phase inversion induced by immersion precipitation technique. Zeta potential demonstrated that covalent functionalization of GO with APTS was favorable for their homogeneous dispersion in organic solvents. SEM images showed that very large channel appeared in top-layer by the addition of additives. Furthermore, the PVDF/f-GO membranes exhibited superior hydrophilicity, water flux, BSA flux and rejection rate than nascent PVDF membranes and PVDF/GO membranes. Filtration results indicated that the fouling resistance parameters were significantly declined due to higher hydrophilicity of hybrid membranes. An atomic force microscope (AFM) analysis with a BSA-immobilized tip revealed that the adhesion forces between membrane and foulants increased in the following order: PVDF/f-GO < PVDF/GO < PVDF. After a ternary cycle BSA solution inner fouling process, PVDF/f-GO membranes exhibited higher water flux recovery ratio (FRR) value than that of PVDF/GO. Meanwhile, tensile strength and elongation-at-break of PVDF/f-GO membranes were increased by 69.01% and 48.38% compared with those of PVDF/GO membranes, which is believed to be attributed to the strong interfacial interaction between f-GO and matrix by covalent functionalization of GO. As a result, GO functionalization will provide a promising method to fabricate graphene-based hybrid membranes with effective reinforced permeation, antifouling and mechanical performance.

© 2014 Elsevier B.V. All rights reserved.

## 1. Introduction

Polymeric material polyvinylidene fluoride (PVDF) is commonly used in ultrafiltration membrane fields because of its good thermal stability, easily-controlled morphology and high porosity [1,2]. However, the application of PVDF in water treatment is restricted due to its hydrophobicity which leads to severe membrane fouling and decline of permeability [3,4]. Subsequently, considerable effort has been devoted to improving hydrophilicity and fouling resistant properties of PVDF membranes, including addition of additives (e.g. siloxane [5] and hydrophilic carbon materials such as carbon nanotubes [6]), chemical modification of surface and bulk membranes

and preparation of amphiphilic polymer blends [7–9]. Recently, graphene derivatives have also become ideal candidates for polymer reinforcement on account of their unique architecture and superior performance. Correspondingly, it can be incorporated into ultrafiltration membranes to optimize targeted properties, such as high water permeability, high salt rejection and better antifouling performance, by the solution-blending method [10,11]. In our previous work, we have also simply investigated the influence of low-dimensional carbon materials (including carbon nanotubes and graphene oxide) on permeation and antifouling performances of ultrafiltration membranes [12,13]. However, graphene derivatives themselves have their shortcomings in numerous applications. One is the homogeneous dispersion which is restricted due to their strong tendency to aggregation [14,15]. Thus, permeation and antifouling performances of graphene-based ultrafiltration membranes may be limited by the aggregation of graphene sheets. Another is that the incorporation of graphene in membranes may cause the decline of the mechanical

\* Corresponding author. Tel./fax: +86 22 83955231.

\*\* Corresponding author. Tel./fax: +86 22 83955051.

E-mail addresses: [xuzhiwei@tjpu.edu.cn](mailto:xuzhiwei@tjpu.edu.cn) (Z. Xu),  
[qianxiaoming@tjpu.edu.cn](mailto:qianxiaoming@tjpu.edu.cn) (X. Qian).

strength of membranes, which is attributed to the bad interfacial interaction between graphene and polymer matrix [16,17]. As a result, the modification of graphene derivatives for the improved performance of ultrafiltration membranes needs to be investigated on the basis of our previous work. Additionally, fouling mechanism and interaction behavior of membrane-foulant as well as the functional mechanism of additives in mechanical properties were not studied fully.

As we all know, covalent functionalization on the surface of graphene is one strategy for fabricating graphene-based polymer composites, which is an effective method to improve interfacial interaction between graphene and polymer matrix [16–18]. Graphene oxide (GO) has abundant functional groups on the surface including hydroxyl, epoxide and carboxyl [17], which provide the reactive site for covalent functionalization. Chemical functionality significantly alters Vander Waals interaction among nanofiller aggregates, making them easy to be dispersed in the polymer matrix. Moreover, functionalized GO can tightly intertwine with PVDF matrix due to their long polymer chains which are expected to penetrate into the matrix. As a result, the covalent functionalization not only makes the dispersibility of GO better but also enables the interfacial interaction between graphene and matrix stronger [17,19]. Hence, we can expect that integrating functionalized graphene oxide in membranes will enhance the hybrid ultrafiltration membrane antifouling performance and mechanical strength greatly. Besides, to the best of our knowledge, the antifouling performance ameliorated by GO functionalization has not been reported till now, and for the first time, the effects of long polymer chains on GO surface on the alleviative fouling behavior and enhanced mechanical strength for hybrid ultrafiltration membranes are investigated fully.

Based on our previous work, the present paper addresses the above-mentioned issue by introducing chemically functionalized GO which was modified by 3-aminopropyltriethoxysilane (APTS). Subsequently, the APTS-functionalized GO (f-GO) and GO with different ratios are incorporated into PVDF matrix via phase inversion induced by the immersion precipitation technique. APTS has a wealth of hydrophilic long polymer chains which can penetrate into and entangle with PVDF matrix. As a result, a significant improvement in membrane performance was achieved because of the better dispersion of f-GO in PVDF matrix as well as the strong interfacial interaction between them.

## 2. Experimental

### 2.1. Materials

The PVDF (FR904) was purchased from Shanghai 3F New Materials Co. Ltd. China. N,N-dimethylacetamide (DMAc, > 99.5%, reagent) and

polyvinyl pyrrolidone (PVP) were purchased from Tianjin Weichen Chemical Reagent Co. Ltd. China. N,N'-dicyclohexyl-carbodiimide (DCC, 99%) and 3-aminopropyltriethoxysilane (APTS, 99%, 0.942 g mL<sup>-1</sup>) were of analytical grade and obtained from Aldrich. Graphite powder, concentrated sulfuric acid (98%), sodium nitrate, potassium permanganate, 30% H<sub>2</sub>O<sub>2</sub> solution and hydrochloric acid were purchased from Sinopharm Chemical Reagent Co. Ltd. (Shanghai, China). Distilled water was used as the nonsolvent for polymer precipitation.

### 2.2. Preparation of graphene oxide and silane-functionalized graphene

Graphite oxide powders were prepared by improved Hummers' method [20]. Then the powders were suspended in pure water (1 mg mL<sup>-1</sup>) and sonicated for 2.5 h to generate a GO suspension. Subsequently, the aqueous GO suspension was frozen into an ice cube in a refrigerator (258.15 K) for 8 h and then was freeze-dried using a FD-1A-50 lyophilizer (Boyikang Co. Ltd., China) with a condenser temperature of 223.15 K at an inside pressure of less than 20 Pa. After 48 h lyophilization and 48 h vacuum drying (318.15 K) process, low-density, loosely packed GO powders were finally obtained. As is well known, GO contains hydroxyl, carboxyl and carbonyl groups on their basal planes and edges, which could provide active sites to react with APTS, as illustrated in Fig. 1. Briefly, GO (100 mg) and DCC (50 mg, as cat.) were dispersed in APTS (50 ml) and followed by ultrasonication for 1 h, and the black and homogeneous mixture was stirred and heated to 348.15 K for 12 h. Afterwards, the resulting f-GO were centrifuged, washed with pure water and then dried under vacuum.

### 2.3. Preparation of membranes

All the membranes were prepared by classical phase inversion method using PVDF and PVP as solute material, DMAc as solvent, GO and f-GO as additives, and distilled water at room temperature as nonsolvent coagulation bath. GO or f-GO (0, 0.5, 1 and 2 wt% based on the weight of PVDF) was first imported into DMAc solvent (84 g), and then the solution was sonicated for 30 min (40 kHz) before addition of PVP (1 g) and PVDF (15 g) powders. Casting solution was then mechanically stirred at 323.15 K for at least 24 h. After fully degassing, the casting solution was spread onto clean glass plates with 200 μm gap and then immersed into coagulation bath (distilled water) for 30 min. After peeling off from glass plates, the resultant membranes were rinsed in distilled water before ultrafiltration tests. In order to identify these membranes easily, it was denoted as PVDF, P/GO and P/f-GO respectively.

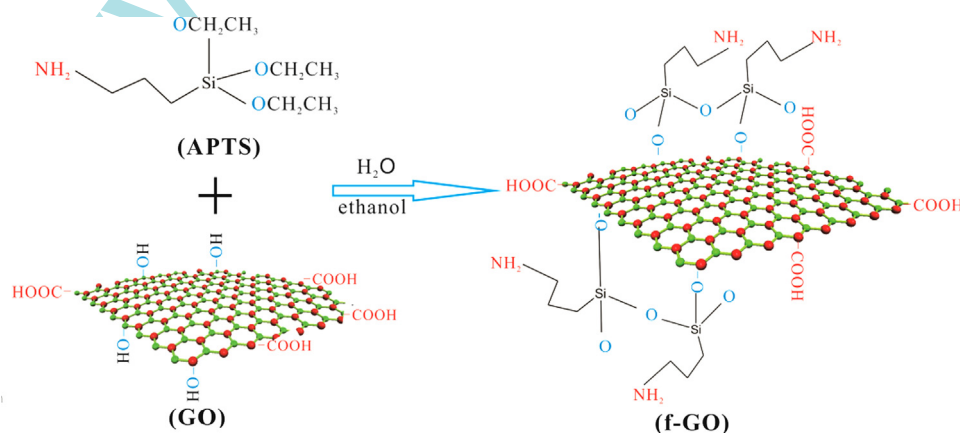


Fig. 1. Illustration of the reaction between GO and APTS.

## 2.4. Characterization of GO and f-GO

Surface morphology of GO and f-GO was examined using atomic force microscope (AFM), and the samples were dispersed by sonication in a mixture of dimethyl formamide, then dried and tested under non-contact mode. Zeta potential was performed using a Delsa Nano instrument and the details are given in Supporting information (Section S2).

## 2.5. Characterization of membranes

### 2.5.1. Structure and functionality

The existence of GO and f-GO in ultrafiltration membranes was characterized by Fourier-Transform Infrared spectroscopy (FTIR). Membrane porosity was determined according to its dry-wet weight. The membranes in distilled water were weighed after mopping. Then the wet membranes were placed in an air-circulating oven at 333.15 K for 24 h before measuring the dry weight. Porosity of membranes was calculated as follows [21]:

$$\varepsilon = \frac{\omega_1 - \omega_2}{A \times l \times d_w} \times 100\% \quad (1)$$

where  $\omega_1$  is the weight of wet membranes;  $\omega_2$  is the weight of dry membranes;  $A$  is the membrane effective area ( $\text{m}^2$ ),  $d_w$  is the water density ( $0.998 \text{ g cm}^{-3}$ ) and  $l$  is the membrane thickness (m). Guerout–Elford–Ferry equation (Eq. (2)) was utilized to determine membrane mean pore radius ( $r_m$ ) on the basis of the pure water flux and porosity data [22]:

$$r_m = \sqrt{\frac{(2.9 - 1.75\varepsilon) \times 8\mu l Q}{\varepsilon \times A \times TMP}} \quad (2)$$

where  $\mu$  is the water viscosity ( $8.9 \times 10^{-4} \text{ Pa s}$ ),  $Q$  is the volume of the permeate pure water per unit time ( $\text{m}^3 \text{ s}^{-1}$ ) and  $TMP$  is the operation pressure (0.1 MPa).

Membrane microstructures were observed under a field emission SEM (Quanta 200, Holland). The cross-sections were prepared by fracturing the membranes at the temperature of liquid nitrogen. All specimens were coated with a thin layer of gold before being observed using SEM.

Viscosities of the casting solutions with different additives were measured using a BROOKFIELD viscometer (DV-1 Prime, America) and the details are given in Supporting Information (Section S3). Pore-diameter distributions were obtained according to previously reported methods [23]. The details are given in Supporting Information (Section S4).

To determine the stability of the hydrophilicity of membranes, the membranes were stirred infrequently changed pure water for 3 weeks and then dried in air. Contact angle (CA) of membranes was recorded by a water contact angle system (JC2000D2). Five different points of every sample were measured and the CA value was the average of these measurements. The solid–liquid interfacial free energy of hydration of membranes was also determined by following Young–Dupré equation [24]:

$$-\Delta G_{SW} = (1 + \cos \theta) \gamma_W^{TOT} \quad (3)$$

where  $\theta$  is the average contact angle and  $\gamma_W^{TOT}$  ( $=72.8 \text{ mJ m}^{-2}$  for pure water at 298.15 K) is the liquid surface tension. The free energies of hydration ( $\Delta G_{SW}$ ) of membranes with water were calculated in order to quantify their relative “hydrophilicity” [25].

### 2.5.2. Separation and antifouling performance

Permeation flux and rejection of membranes were measured by ultrafiltration experimental equipments. The sample membranes were immersed in pure water before measurement. Measuring protocol was depicted as follows: for the first 30 min, the membranes were compacted at 0.1 MPa to get a steady flux, and then

the flux was recorded at 0.1 MPa every 5 min, and at least 5 readings were collected to obtain an average value. After this, pure water was changed to  $1 \text{ g L}^{-1}$  bovine serum albumin (BSA) solution. The experiment was also conducted under the feed pressure of 0.1 MPa, and membranes were pre-pressurized for 30 min before test. Concentrations of BSA in the permeation and feed solution were measured by UV-spectrophotometer (Shimadzu UV-2450, Japan). Permeation flux and rejection were defined using the following equations respectively:

$$J = \frac{Q}{A \times T} \quad (4)$$

$$R = \left(1 - \frac{C_p}{C_f}\right) \times 100\% \quad (5)$$

where  $J$  is the permeation flux of membrane for pure water ( $\text{L m}^{-2} \text{ h}^{-1}$ ),  $Q$  is the volume of permeate pure water (L),  $A$  is the effective area of membrane ( $\text{m}^2$ ) and  $T$  is the permeation time (h).  $R$  is the rejection to BSA (%), and  $C_p$  and  $C_f$  are the concentrations of BSA in the permeation and feed solution, respectively (wt%).

In the dead-end filtration, flux decline can be caused by several factors, such as adsorption between membrane and solutions, cake or gel formation, concentration polarization, and membrane hydraulic resistance. Resistance-in-series model is particularly applicable to the analysis of flux decline of BSA [26]. It was described as follows:

$$J_{tot} = \frac{TMP}{\mu R_{tot}} \quad (6)$$

where  $J_{tot}$  is the flux ( $\text{L m}^{-2} \text{ h}^{-1}$ );  $TMP$  is the transmembrane pressure (0.1 MPa);  $\mu$  is the viscosity of water at room temperature ( $1.005 \times 10^{-3} \text{ Pa s}$ ), and  $R_{tot}$  is the total filtration resistance.

The resistance-in-series model combines various resistances that cause flux decline was as follows:

$$R_{tot} = R_m + R_g + R_c + R_a = \frac{TMP}{\mu J_{tot}} \quad (7)$$

where  $R_m$  is the membrane hydraulic resistance, which can be determined by water flux of the clean membrane,  $R_g$  is the cake layer resistance,  $R_c$  is the concentration polarization resistance and  $R_a$  is the adsorption resistance. All the procedures were measured as follows:

$$R_m = \frac{TMP}{\mu J_{mem}} \quad (8)$$

$$R_g = \frac{TMP}{\mu J_{pore}} - R_m - R_a \quad (9)$$

$$R_a = \frac{TMP}{\mu J_{irr}} - R_m \quad (10)$$

First, membrane hydraulic resistance  $R_m$  was calculated by measuring the flux of pure water through a clean membrane ( $J_{mem}$ ). After this, the BSA solution was filtrated and the permeate flux ( $J_{tot}$ ) was recorded during the whole process. According to Eq. (7),  $R_{tot}$  could be calculated during this process. Then the feed broth was replaced by pure water and the water flux in this situation  $J_{pore}$  was recorded. Subsequently, the membranes were flushed with pure water and cleaned by removing the gel layer, and then the water flux  $J_{irr}$  was determined. All experiments were conducted at 298.15 K and under the feed pressure of 0.1 MPa. Similarly, the membranes were pre-pressured at 0.1 MPa for 1 h before measurement, and then the experiments were measured. Thus, all membrane resistances can be quantified by Eqs. (6)–(10).

In order to evaluate fouling-resistant ability of membranes, flux recovery ratio (FRR) was calculated after surface and inner fouling

by BSA solution using the following expression:

$$FRR = \frac{J_{w1}(\text{or } J_{w2})}{J_{mem}} \times 100\% \quad (11)$$

where  $J_{mem}$  is the pure water flux of sample membrane before fouling and  $J_{w1}$  (or  $J_{w2}$ ) is the pure water flux after fouling. In the process of surface fouling, the pure water flux of virgin membrane ( $J_{mem}$ ) is measured as mentioned in Section 2.5.2, and then the sample membrane was kept soaking in protein solution for 3 h under stirring. Subsequently, the surface fouled membrane was taken out from protein solution and washed many times by pure water. Then the pure water flux of surface fouled membrane ( $J_{w1}$ ) was measured. In the process of inner fouling, after pure water filtration ( $J_{mem}$ ) experiment, the tank was refilled with  $1 \text{ g L}^{-1}$  BSA solution and the flux ( $J_p$ ) was calculated ( $J_p$ =the flux of BSA solution with a clean membrane). After BSA ultrafiltration for 180 min, the membrane was taken out from the cell, then washed many times by pure water and again the pure water flux of the membrane was measured ( $J_{w2}$ ). Similarly, the second and third surface fouling and inner fouling were measured after the first fouling experiments respectively.

To analyze the fouling process in detail, several equations were used to describe the fouling resistance of membranes. The total flux decline ratio ( $R_t$ ), reversible flux decline ratio ( $R_r$ ), and irreversible flux decline ratio ( $R_{ir}$ ) were defined and calculated as follows:

$$R_t = \left(1 - \frac{J_p}{J_{mem}}\right) \times 100\% \quad (12)$$

$$R_r = \left(\frac{J_{w2} - J_p}{J_{mem}}\right) \times 100\% \quad (13)$$

$$R_{ir} = \left(\frac{J_{w0} - J_{w2}}{J_{mem}}\right) \times 100\% \quad (14)$$

### 2.5.3. Interaction force between membrane surface and AFM tip

Interaction forces between membrane surface and a BSA-immobilized tip were measured by an AFM (CSPM5500). The AFM tip was modified according to the procedure described elsewhere [27]. We used BSA for the immobilization of a protein on the AFM tips. A  $\text{Si}_3\text{N}_4$  cantilever was treated with oxygen plasma (150 W, 60 s) and then chemically modified with 10 mM 3-aminopropyltriethoxysilane toluene solution for 2 h at room temperature. This amine-terminated AFM tip was further immersed in the solution of glutaraldehyde (50% in  $\text{H}_2\text{O}$ ) for 30 min, which was followed by reaction with the BSA in phosphate buffer solution (PBS, pH=7.4) for 40 min. Then, the tip was washed with PBS and subsequently stored in PBS.

As membrane surface approached the BSA-immobilized AFM tip, an interaction was generated between the tip and membrane surface, inducing a cantilever deflection. By multiplying the spring constant of the cantilever by the deflected distance (change in photodiode signals), the intermolecular force between the BSA-immobilized AFM tip and membrane surface could be calculated. The force could be detected in the same manner when the surface was retracted. A force–extension curve then could be constructed from these measurements. We used a spring constant of  $0.2 \text{ N m}^{-1}$ , supplied by the manufacturer. A speed of  $0.1 \mu\text{m s}^{-1}$  was applied to obtain the force–extension curves during approach and retraction of membrane surface from the BSA-immobilized tip. All experiments were carried out in PBS at room temperature. Approximately 50 approach/retract cycles were performed for each polymer surface collected from at least 5 positions on the sample.

### 2.5.4. Mechanical strength tests

The membrane strength was measured by testing the tensile strength and elongation-at-break of membrane coupons ( $150 \text{ mm} \times 20 \text{ mm} \times 0.22 \text{ mm}$ ) with a Instron 3369 tensile tester. All the tensile tests were carried out at a stepper motor speed of  $10 \text{ mm min}^{-1}$  at room temperature, and the thickness of the sample was measured according to the vernier caliper. Results were averaged from five samples.

## 3. Results and discussion

### 3.1. Morphology, functional groups and dispersity of GO and f-GO

In order to measure the thickness of GO and f-GO materials, AFM observations were conducted. The tapping-mode AFM images of GO and f-GO dispersed in DMF are presented in Fig. 2. From cross-section analysis, we could find that GO had a height of  $1.09 \pm 0.14 \text{ nm}$  (Fig. 2(c)), corresponding well with the reported thickness found in previous literature [28]. Fig. 2(d) revealed that the average thickness of f-GO sheets was  $1.57 \pm 0.19 \text{ nm}$ , which was thicker than that of GO. The increase of f-GO in thickness was attributed to the presence of functionalized silane chains grafted on the graphene sheets. Similar results have also been observed for the thickness of well exfoliated functionalized graphene sheets by AFM measurement [16,17].

X-ray photoelectron spectroscopy (XPS) was employed to further explore the interaction between GO and APTS. Fig. 3 shows the survey data of samples and higher resolution spectra of Si2p areas. The survey (a) of GO shows the absence of any detectable amounts Si and N1s, while Fig. 3(b) depicts Si and N1s components, indicating that covalent functionalization of GO by APTS successfully occurred. The higher resolution data of C1s area of GO and f-GO are shown in Fig. 3(c) and (d), respectively. Comparing Fig. 3(c) with (d), we can find out that C–N and C–Si bonds appeared in f-GO. This result follows from the fact that APTS reacted with GO (Fig. 1), and the newly formed C–N and C–Si bonds of APTS are attached on the GO surface. It is affirmed that APTS has reacted with GO.

Zeta potential has been used for the characterization of the dispersion of carbon nanomaterial suspension, and it should be noted that zeta potential can be related to the stability of colloid dispersion and a high zeta potential will confer stability [29]. As shown in Fig. S1, pristine GO dispersions in DMAc are not stable and tend to agglomerate. However, in the case of f-GO materials, the zeta potential becomes significantly more negative ( $-48.69 \pm 2.46 \text{ mV}$ ), suggesting the higher stability of f-GO. In addition, it was further illustrated by the photographs of GO and f-GO dispersion (cf. Fig. S1). This striking contrast obviously showed that surface-grafting can significantly improve the dispersion status of GO in organic phase.

### 3.2. Structure, morphologies and functionality of membranes

Fig. S2 (line b–d) shows FTIR spectra of membranes. Compared with the spectra of nascent PVDF membranes, a peak at  $1650 \text{ cm}^{-1}$  is observed, which is attributed to the carboxylic groups of GO and f-GO. This result indicates that blending hydrophilic materials with PVDF matrix could incorporate carboxylic groups in the modified membranes. The same behavior has been observed by addition of oxidized carbon nanotubes to the polymeric membranes [30]. Moreover, compared with P/GO, new peaks at  $1030 \text{ cm}^{-1}$ ,  $2930 \text{ cm}^{-1}$  and  $3300 \text{ cm}^{-1}$  were seen on the P/f-GO membranes. These peaks are attributed to the stretching vibration of Si–O–C,  $-\text{CH}_2-$ , and N–H groups on APTS monomer, supporting that APTS monomer was indeed incorporated into the

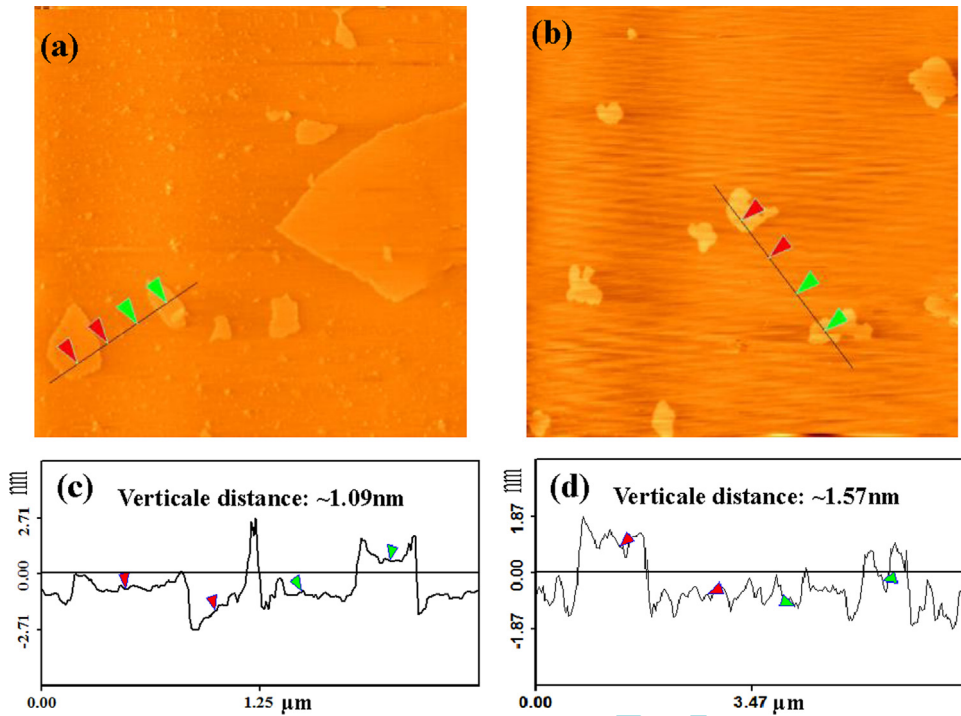


Fig. 2. AFM images of (a) GO and (b) f-GO dispersed in DMF.

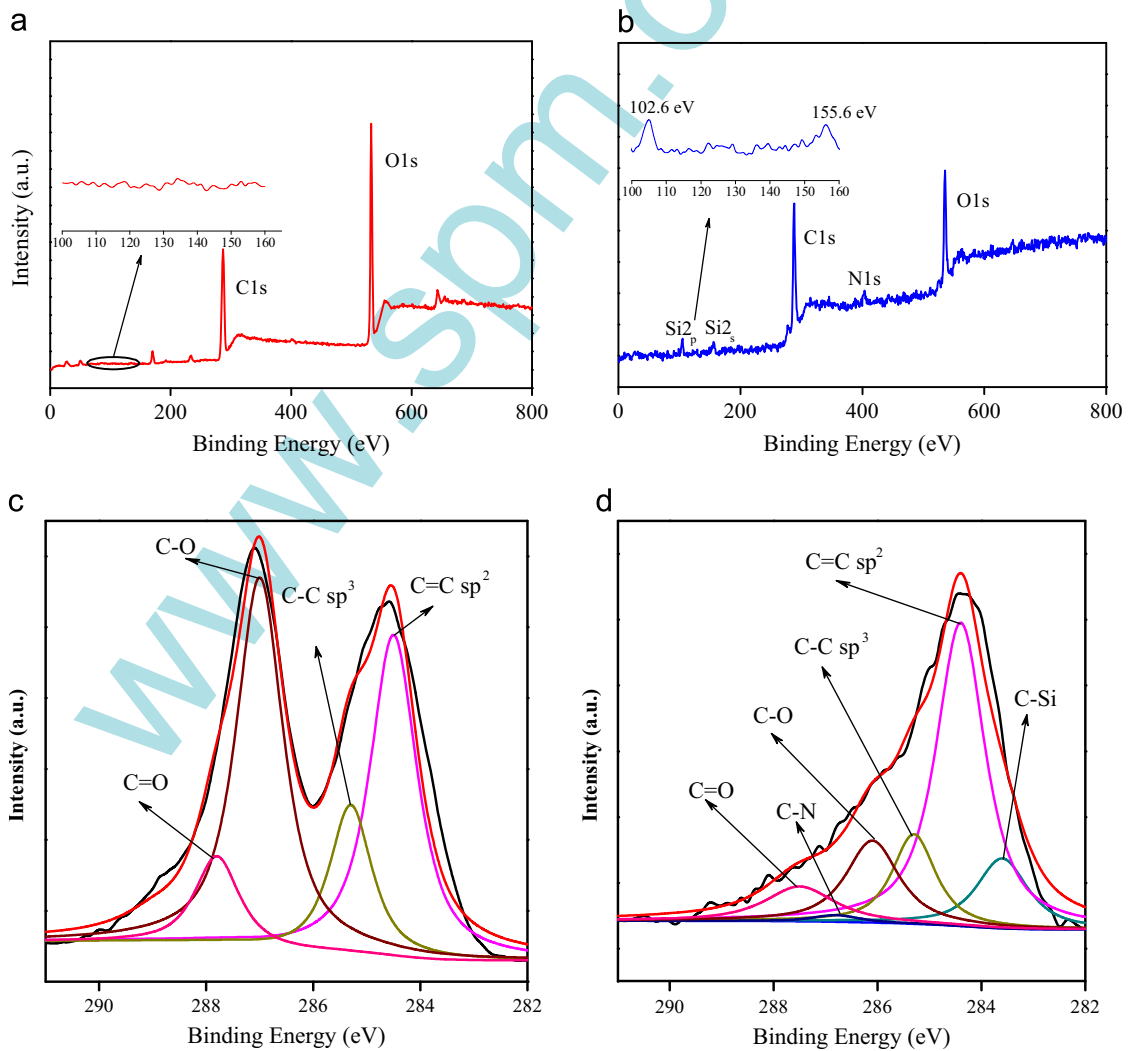
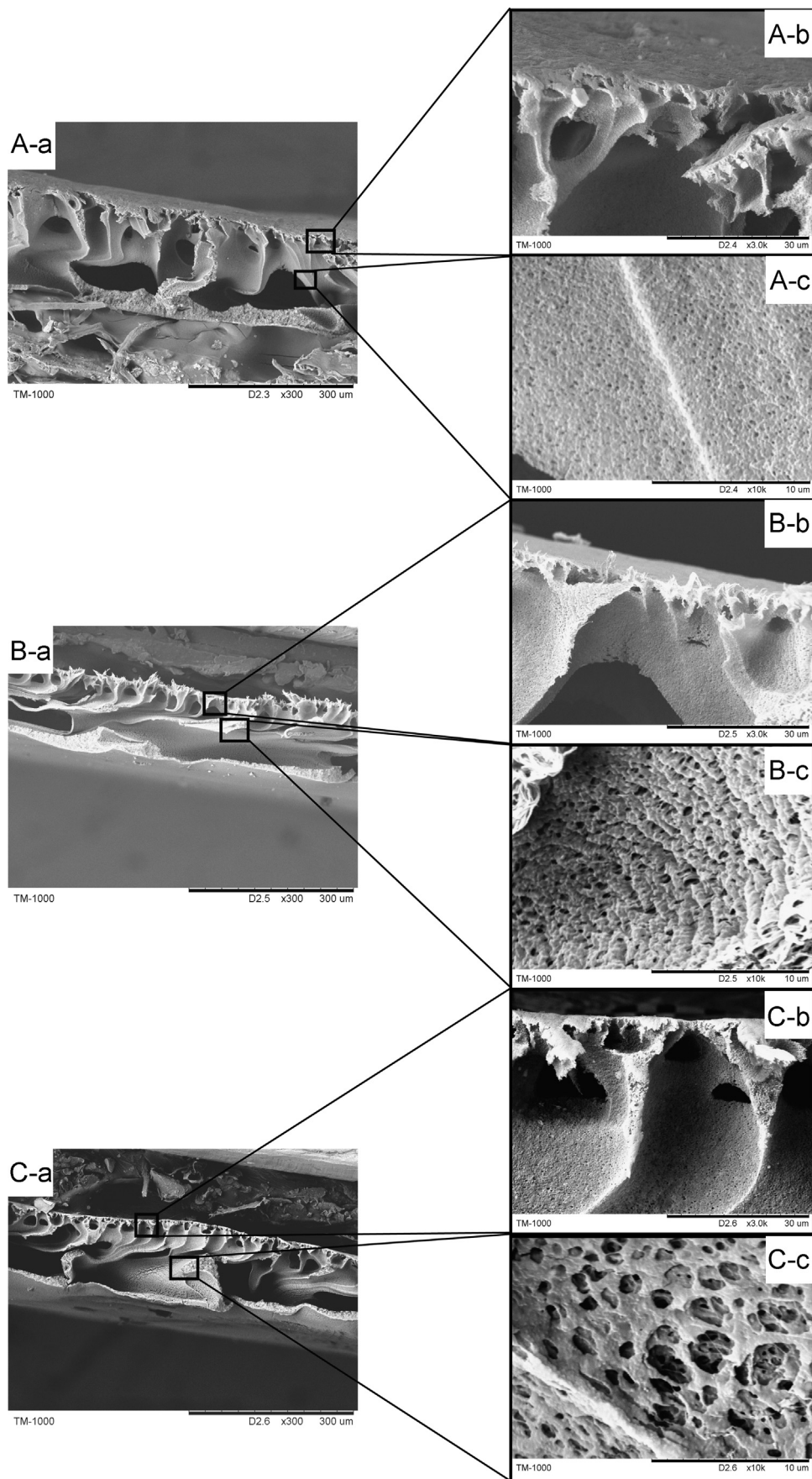


Fig. 3. Survey curves of (a) GO, (b) f-GO (inset: the higher resolution curves of Si area) and higher resolution curves of C1s of (c) GO and (d) f-GO.



**Fig. 4.** Cross-sectional SEM images of (A) nascent PVDF, (B) P/GO (1 wt%), (C) P/f-GO (1 wt%) membranes and their magnified top layer (b) and inner structures (c).

GO via functionalization process. The fact is in agreement with the observed sequence of XPS analysis (Fig. 3).

The SEM images of cross section of nascent PVDF and modified membranes are shown in Fig. 4. The cross-sections (series a) of all membranes presented asymmetric and highly inhomogeneous structure with a selective thin microporous upper skin on large voids and a porous sub-layer cavities. This structure was mainly due to the high mutual diffusivity of water and DMAc [31]. It seemed that the finger-like microvoids turned to be elongated across the thickness, and became wider compared with nascent PVDF membranes. Furthermore, the P/f-GO membranes exhibited the widest finger-like structure. It can be explained by the affinity of f-GO with many types of hydrophilic groups, which increase mass transfer rate between solvent and non-solvent during phase-inversion. Therefore, larger pore channels would form due to the rapid mass transfer [10]. The phenomena undoubtedly benefited the water permeability (cf. Fig. 6) [32]. With respect to inner structure of membranes (series c), the variation of membrane pores in number and size was observed. It could be clearly seen that addition of additives results in the increase of pore number and size in inner structure compared with PVDF membranes. It seems that this change in membrane morphology can be interpreted by the phase separation mechanism during the immersion precipitation. It is obvious that the presence of additives in the solution enhanced thermodynamic instability, which is in favor of phase separation progress. Also, the long chains of APTS are expected to penetrate into the matrix, which further enhanced thermodynamic instability of blend casting solution, so it is inherently prone to phase separation. Thus, the system became less stable and led to the quicker liquid–liquid phase separation with more porous structure of cross-section [33].

Fig. 5(a) presents overall porosity and mean pore size of membranes. The overall porosity and mean pore size of membranes are initially increased by incorporation of low amount of GO and f-GO and then, reduced by more addition of the additives. The phenomena are similar to other reports [34,35]. Obviously, P/f-GO membranes presented better performance than P/GO membranes and nascent PVDF membranes. As reported in previous reports [36], mixing hydrophilic nanoparticles with the matrix of polymer could increase the amorphous nature of membranes. Together with the fast exchange of solvent and non-solvent in the phase inversion process, the overall porosity of modified membranes was improved [22]. The incorporation of GO and f-GO increases the solution thermodynamic instability in the gelation bath (nonsolvent), which promotes a rapid phase demixing, resulting in large pore formation in low amount of the additives on the membrane surface [32]. On the other hand, decrease of the mean pore size in high content of additives is

probably due to the increased viscosity (cf. Fig. S3) of blend solution by addition of additives [37]. The viscosity of blend solutions increases along with the content of the additives. As a result, the increase of the viscosity typically delays the exchange of solvent and nonsolvent as well as suppresses the formation of large pore size. Similarly, Xu et al. [38] have proved that porosity of modified membranes decreased with high content of additives, and they explained the fact by the increase in total solid content. Pore size distributions are also considered to be the key specification factors for porous membrane. It was shown in Fig. S4 that the size of predominant pore in modified membrane was bigger than that of nascent PVDF membranes. The pore size distribution results were well in agreement with the mean pore size analysis. Mean pore size, porosity and pore size distribution might play a role in raising membrane permeability which was discussed in the following sections.

Surface hydrophilicity of membranes is usually expressed in terms of contact angle for a water drop on the membrane surface to evaluate the tendency of water to wet membrane surface. The contact angle of nascent PVDF membranes is  $71.0^\circ$  because of its intrinsic hydrophobicity characteristic (cf. Fig. 5(b)). Value of modified membranes was lower than that of PVDF, which is consistent with the FTIR spectra [39]. This might play a favorable role in elevating flux recovery of modified membranes [40]. The improved hydrophilicity can be explained by the fact that hydrophilic GO and f-GO migrated spontaneously to the membrane surface to reduce the interface energy during the phase inversion process, making membrane surface hydrophilic [41]. In general, contact angle is influenced by chemical composition of the surface of membrane. In the case of modified membranes, the presence of functional groups of additives effectively serve to lower contact angle [24]. Furthermore, the better dispersion of f-GO makes the oxygen-containing functional groups fully exposed on the membrane surface which definitely render them play their role effectively. From Wenzel model [42], we can see that as for hydrophilic materials, the large surface roughness will achieve a low contact angle. The P/GO membranes had larger surface roughness, while their contact angles were larger than P/f-GO membranes. It indicated that the effects of f-GO on membrane hydrophilicity were remarkable. As a result, the P/f-GO membranes exhibit better hydrophilicity than P/GO membranes. However, by embedding 1 wt% of additives, the contact angle of P/GO and P/f-GO membranes decreased to the lowest, and a further increase of additives (more than 1 wt%) did not result in decrease in the contact angle. The reason can be explained as follows: the additives with high content were not evenly distributed in casting solution, which reduced the effective surface of additives and the functional groups on the surface of modified membranes [43,44]. Additionally, the

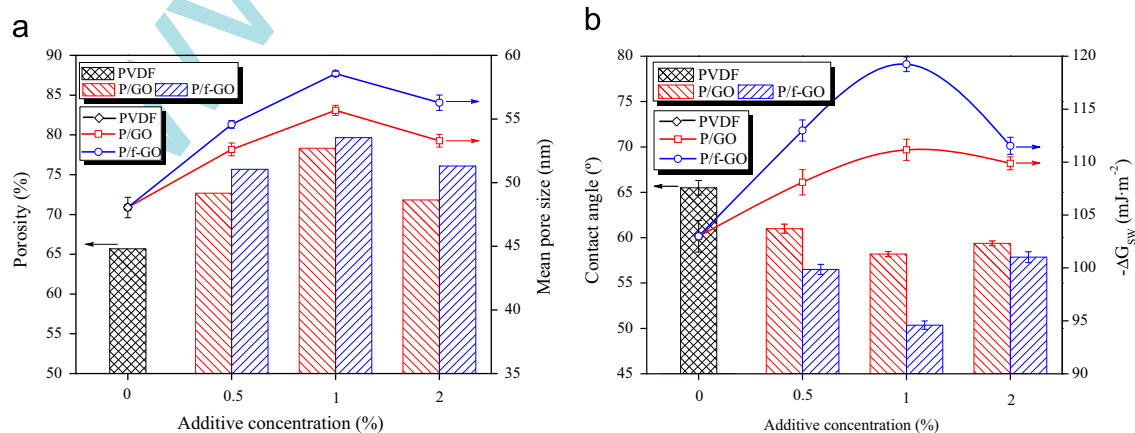


Fig. 5. (a) Porosity, mean pore size and (b) static water contact angles, interfacial free energy of hydration of various membranes.

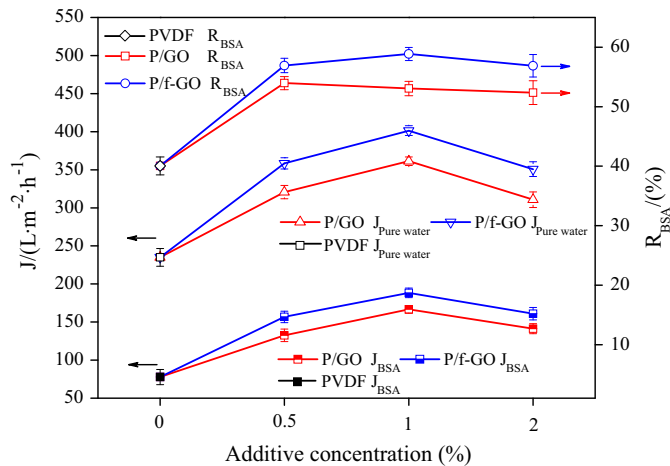


Fig. 6. BSA flux, pure water flux and BSA rejection of various membranes.

free energy of hydration ( $\Delta G_{\text{SW}}$ ) was also used to evaluate the modification of the relative hydrophilic character of membranes [25]. The values of  $-\Delta G_{\text{SW}}$  (cf. Fig. 5(b)) showed that modified membranes, especially P/f-GO membranes, were slightly more hydrophilic than other membranes [24,45].

As shown in Fig. 6, influence of addition of GO and f-GO on the permeability and rejection of membranes was examined. The BSA and pure water flux results shown that 1 wt% additives/PVDF membranes had the highest flux. However, higher additive concentration (2 wt%) in the membranes led to a decrease in flux because of either the reduced mean pore size or the plugged membrane pores induced from the agglomeration of additives [46]. The same behavior was reported by Liu et al. [37] and Qin et al. [47]. In detail, the nascent PVDF membranes give the lowest BSA flux and pure water flux around  $78 \text{ L m}^{-2} \text{ h}^{-1}$  and  $235 \text{ L m}^{-2} \text{ h}^{-1}$ , and the P/GO membranes (1 wt%) up to  $166.67 \text{ L m}^{-2} \text{ h}^{-1}$  and  $361.24 \text{ L m}^{-2} \text{ h}^{-1}$ . The phenomenon was ascribed to the increased hydrophilicity which was caused by oxygen-containing functional groups on additives [48,49]. Generally, GO could attract water molecules inside the membrane matrix and promoted them to pass through membranes and accordingly enhanced the permeability [44]. Since f-GO has higher affinity to water than GO, the penetration velocity of water (non-solvent) into the membranes were increased during phase inversion. Furthermore, the increased solution thermodynamic instability by addition of f-GO also resulted in enhancing the diffusion velocity of solvent (DMAc) from membranes to water [34]. These phenomena lead to big pore size of modified membranes (cf. Fig. 5 (a)) which play a positive role for enhanced permeability. Consequently, the BSA flux and pure water flux of P/f-GO (1 wt%) amount to  $188.36 \text{ L m}^{-2} \text{ h}^{-1}$  and  $401.39 \text{ L m}^{-2} \text{ h}^{-1}$ , respectively. In the case of 1 wt% GO and f-GO content, the highest flux of modified membranes can be explained as follows. (a) As shown in Fig. 5(a) and (b), the addition of 1 wt% additives accounts for the highest improvement in mean pore size and hydrophilicity of membranes. The increase of membrane mean pore size and membrane hydrophilicity facilitates water molecule penetration through membranes, which serve to enhance the flux subsequently [50]. (b) Effects of additives on the membrane morphology would also affect the permeation properties. The larger channel of upper side and the porous inner structure of modified membranes (cf. Fig. 4) undoubtedly benefited the water permeability as shown in Fig. 6 [32]. The rejection rate can also be improved with the addition of additives. For either P/GO membranes or P/f-GO membranes, the BSA rejection rate was as high as above 55%, compared to 40% of the nascent PVDF membranes. This phenomenon

Table 1

Filtration resistances of nascent PVDF and 1 wt% additive mixed PVDF membranes.

Membranes	BSA filtration resistance ( $10^7 \text{ m}^{-1}$ )					
	$R_m$	$R_g$	$R_a$	$R_c$	$R_{\text{tot}}$	$R_g/R_{\text{tot}}$
PVDF	7.20	15.12	3.38	4.29	30.00	50.40
P/GO	3.91	1.07	0.83	0.40	6.21	17.23
P/f-GO	2.81	0.59	0.79	0.43	4.62	12.77

can be explained by the complete absorptive action caused by adding carbon nanomaterials [51]. At the same time, the surfaces of modified membranes were hydrophilic due to strongly bound water molecules that can effectively prevent BSA molecules from passing through membrane surfaces [52]. It generally accepts that rejection of ultrafiltration membranes was based on the sieving mechanism which was related to the pore size of membranes and molecular weight of the solute [53]. When GO concentration was 0.5 wt%, the rejection of P/GO membranes achieve the highest. This result could be explained by the fact that the increase of pore size had a negative effect on rejection when GO concentration was as high as 1 wt% and 2 wt%. Furthermore, the rejection changed slightly with the increase of f-GO concentration and had maximum at 1 wt% f-GO. It can be responsible for the highest hydrophilicity of membranes [44] and the better dispersion of f-GO (cf. Fig. S1). However, the rejection of modified membranes decreased slightly when additives were more than 1 wt%, which suggests that the influence of surface hydrophilicity on rejection possibly outweigh mean pore size.

### 3.3. Fouling behavior of membranes

#### 3.3.1. Fouling mechanism and interfacial adhesion forces

Resistance-in-series model was applied to analyze resistances that lead to flux decline during ultrafiltration process. Fouling resistance and the  $R_g/R_t$  ratios are presented in Table 1. Results indicated that flux decline should be largely attributed to the cake layer which deposited on the membrane surface. It can be seen that  $R_g$  value for all modified membranes, ranging from  $0.59 \times 10^7 \text{ m}^{-1}$  for P/f-GO to  $1.07 \times 10^7 \text{ m}^{-1}$  for P/GO, was significantly different from that of nascent membranes ( $15.12 \times 10^7 \text{ m}^{-1}$ ). It is further supported by the  $R_g/R_t$  ratios which decreased from 50.4% in nascent membranes to 17.23% and 12.77% in P/GO and P/f-GO, attributing to the reduction in hydrophobic interaction between membrane and foulants [54].

Fouling is governed by cake layer on the membrane surface. Thus, the adhesion force of foulants against the surface of membranes is an important parameter that allows direct assessment of protein adsorption behavior at the interface. The interaction force between membrane and foulants was investigated by AFM (cf. Fig. 7). Previous results demonstrated by others also have shown that the magnitude of adhesion force correlates well with the fouling propensity of membranes and surfaces in the presence of organic foulants [55,56]. Fig. 7 (a)–(c) shows that the adhesion forces between membrane and foulants increased in the following order: P/f-GO < P/GO < PVDF. Upon considering the results of flux curves of membranes, it is clear that, the stronger the adhesion force of the membrane–foulant, the more severe flux decline in permeation process (cf. Fig. 6). This suggests that the adhesion force of membrane–foulant could be used to predict the flux decline rate and extent of membrane fouling in the permeation process. The agreement between magnitude of interfacial forces and observed rates of membrane fouling implies that interfacial force measurements between a BSA-immobilized tip and membranes are directly related to the fouling potential of membranes. It also demonstrates that elimination of foulant–membrane adhesion is one key factor in controlling membrane organic fouling [57].

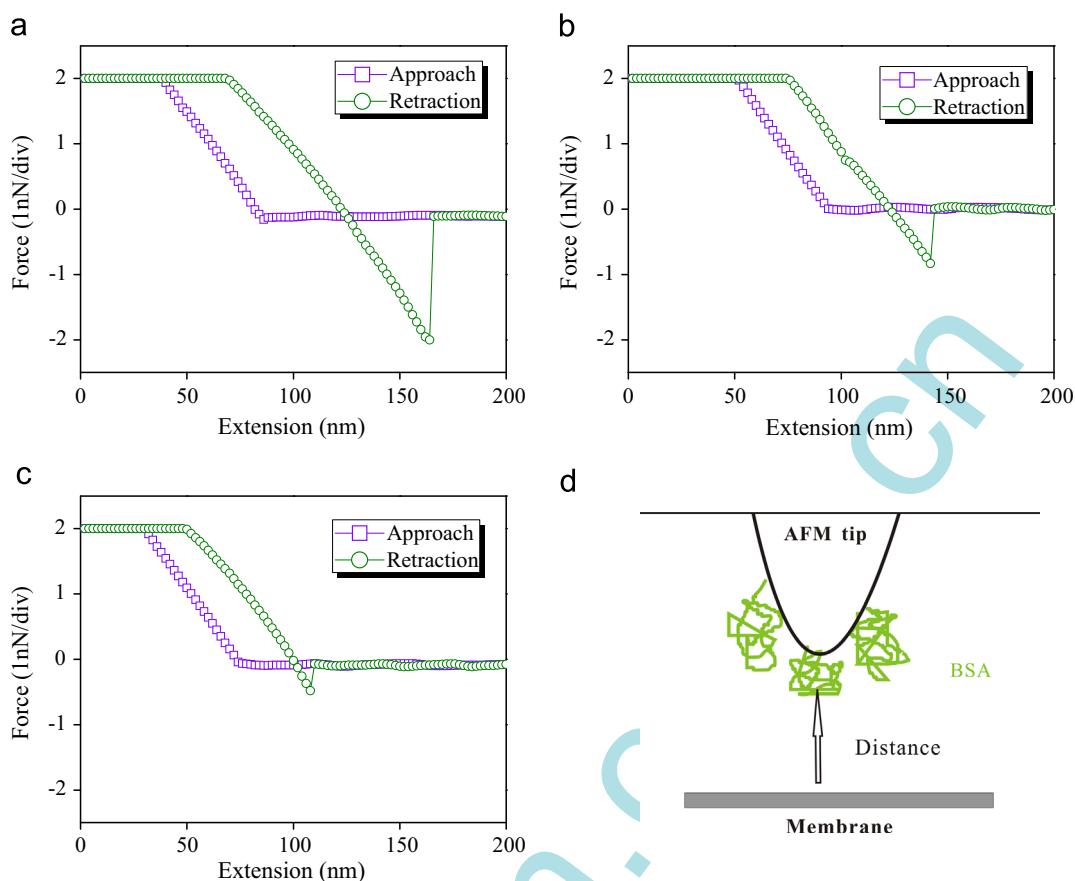
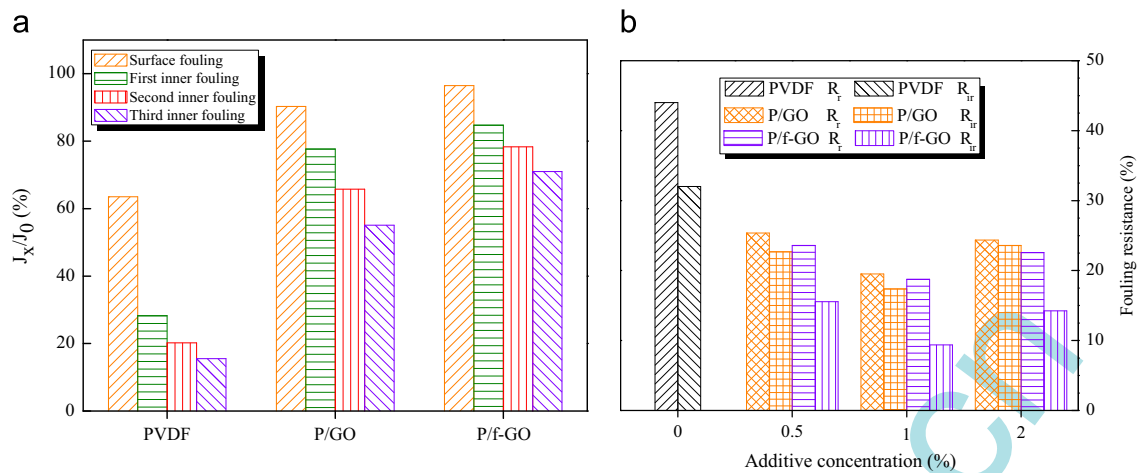


Fig. 7. Force–extension curves recorded with a BSA-immobilized tip against (a) nascent PVDF, (b) P/GO (1 wt%), (c) P/f-GO (1 wt%) and (d) schematic for the measurement of force extension curves between protein-immobilized tips and membranes.

### 3.3.2. Flux recovery rate and the surface roughness

The *FRR* depicted in Fig. 8(a) can obviously present the suitable recycling properties of membranes. The higher *FRR* means better antifouling property for membranes. As shown in Fig. 8(a), the *FRR* of modified membranes is higher than that of nascent membranes, after not only surface fouling but also inner fouling. In detail, after BSA solution surface fouling, the *FRR* of P/GO membranes and P/f-GO membranes was about 1.47 and 1.66 times higher than that of the nascent membranes. Moreover, the *FRR* of P/GO membranes and P/f-GO membranes were approximately 2.26 and 3.28 times after a ternary cycle BSA solution inner fouling process, higher than that of the nascent PVDF membranes. This phenomenon could be explained as follows: protein molecules may be entrapped in the large pores and block the channels, which cannot be removed by hydraulic cleaning for hydrophobic membranes, and thus the water flux after cleaning cannot completely resume to the initial value [58]. Additionally, the P/f-GO membranes have higher *FRR* than P/GO membranes in all cycle permeation process. This could be resulted from the well dispersed f-GO in membrane pore channel which made the entrapment of pollutant in the pores washed away easily by water (cf. Fig. S1). As is well known, hydrophilic membranes mitigate protein adsorption due to the repulsion force from the hydrated layers on the surface. Besides, APTS is a hydrophilic polymer, which could immobilize water molecules in the vicinity of the amino groups during the presence of water. The hydrated layers hinder the protein adsorption and stabilize its folded structure which could guarantee the proteins in external solution contact the surface reversibly, with no obvious conformational change of the proteins [59,60]. As a result, P/f-GO membranes possess better antifouling performance compared with P/GO membranes.

We have investigated the relationship between surface morphology and fouling behavior. As we all know, surface morphology of ultrafiltration membranes plays an important role in determining the characteristics of membrane fouling [61]. It is well established that a membrane with smoother surfaces has greater fouling resistance capability. Fig. S5 shows the three-dimensional surface AFM images of membrane surfaces. Obtained AFM images showed that the mean roughness ( $R_a$ ) of P/f-GO membranes is smaller than that of P/GO membranes. Previous results showed that increased hydrophilicity and lower surface roughness were associated with better antifouling performance [62]. The membrane fouling trend gets larger with roughness due to protein accumulating in the “valleys” of rough membrane surface (cf. Fig. 9). In the initial stages of fouling, foulants accumulated in the valleys of rough membranes, causing severe flux decline [63]. A colloid probe AFM study of a smooth membrane also found that colloid fouling could be greatly reduced if the periodicity of roughness was small enough to prevent penetration of the colloids into the valleys [64]. It is well in agreement with our adhesion force measurements (cf. Fig. 7). The nascent PVDF membranes exhibited weak antifouling performance, while its  $R_a$  is the smallest among all membranes. The phenomena can be explained by the following aspects. It has been mentioned that fouling behavior may be attributed to two factors. One is the improved hydrophilicity of membrane which can reduce membrane fouling. The higher hydrophilicity could cause formation of a water molecule layer on modified membrane surface and retard hydrophobic foulants [65]. After modification by GO and f-GO, the formed hydration layer holds large amount of free water on membranes surface. An overall result also suggests that membrane with hydrophilic additives could induce denser and more stable



**Fig. 8.** (a) Water flux recovery percentage of nascent membranes and (b) 1 wt% additive mixed PVDF membranes after surface and inner fouling by BSA solution and the fouling resistance of different membranes.

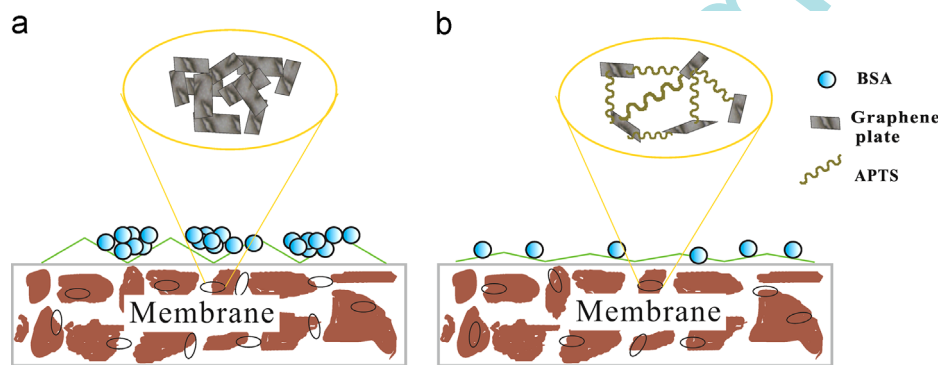


**Fig. 9.** Schematic illustration of states of additives in (a) P/GO and (b) P/f-GO membranes and the relationship between surface morphology and fouling behavior.

hydration layer, which could endow the superior antifouling property [66]. Another one is the surface morphology which is affected by embedding additives with different ratios. In our experiments, comparing nascent PVDF membranes with 1 wt% additives/PVDF membrane, it revealed that the influence of membrane hydrophilicity improved by adding additives on fouling behavior of membranes was probably more significant than that of the surface morphology [67].

### 3.3.3. Fouling resistance of membranes

To understand more about the fouling phenomenon, resistance parameters such as reversible ( $R_r$ ) and irreversible ( $R_{ir}$ ) fouling resistance were calculated and depicted in Fig. 8(b). Reversible protein adsorption led to reversible fouling which could be removed by simple hydraulic cleaning. On the contrary, irreversible fouling was caused by firm adsorption of protein molecules on the surface or entrapment of protein molecules in pores [68]. In Fig. 8(b), the main difference in the fouling resistance of membranes was observed in the  $R_{ir}$  value. This implies that the  $R_{ir}$  dominates the total fouling.  $R_{ir}$  value of nascent PVDF membranes was 48.2% (more than 75% in total fouling) due to its lower surface hydrophilicity. By addition of low amount of GO and f-GO, the  $R_{ir}$  decreased and above 1 wt%, the parameters increased. The  $R_r$  of P/GO and P/f-GO membranes was roughly similar, however, it was higher than that of the nascent PVDF membranes, indicating better detaching of the adsorbed foulants from the modified membrane surface by the washing process. These results indicated that the introduction of GO and f-GO can improve the antifouling capability considerably. P/f-GO membranes have better antifouling

performance comparing with the P/GO membranes. The main reason of the irreversible fouling is trapping and aggregation of the foulants in the membrane pores and “valleys” of membrane surface [69], which are considerably detached from membrane surface by cleaning process. Therefore, role of reduction of surface roughness and increment of hydrophilicity in mitigation of  $R_{ir}$  ratio is all important. As a result, the better antifouling performance of P/f-GO membranes can be explained by the fact that it has higher surface hydrophilicity (cf. Fig. 5(b)) and lower surface roughness (cf. Fig. S5) [34]. The results from above studies suggested that the newly fabricated membranes by embedding GO and f-GO, which had lower  $R_{ir}$  fouling resistance and higher FRR related to the nascent PVDF membranes, could be used as a suitable membrane in the filtration of industrial effluents and treatment of wastewaters.

### 3.4. Mechanical properties of membranes

The mechanical strength of ultrafiltration membranes is a key factor to evaluate their usefulness in practical application. We examined the mechanical strength of all membranes by testing their tensile strength and elongation-at-break. Representative stress-strain curves for the nascent PVDF, P/GO and PVDF/f-GO membranes are plotted in Fig. 10. It is generally accepted that the incorporation of foreign components in porous ultrafiltration membranes will cause the decline of the mechanical strength of membranes [48]. The introduction of GO led to a 6.58% descend in tensile strength compared with nascent PVDF membranes, while it was increased by 57.89% for the P/f-GO membranes. It indicates that the addition of f-GO could contribute to the improvement of the mechanical strength of membranes, however, the incorporation

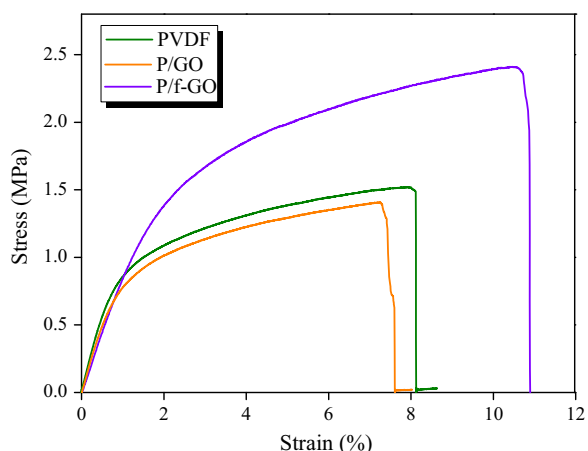


**Fig. 10.** Stress–strain curves of nascent membranes and 1 wt% additive mixed PVDF membranes.

of GO makes the membranes become fragile. The reason why P/f-GO membranes exhibited better strength than P/GO membranes can be attributed to two aspects: the silane chain grafted at the GO surface can prevent stacking and aggregation of GO, and thus improved the dispersion state of the graphene sheets in PVDF matrix; more importantly, the APTS were expected to penetrate into and entangle with PVDF matrix due to its long chains. Consequently, the interfacial interaction between different components became stronger. The results demonstrated that covalent functionalization of GO with APTS played a vital role in determining the mechanical strength of ultrafiltration membranes.

#### 4. Conclusions

Novel PVDF hybrid membranes that contain different proportions of GO and f-GO were prepared successfully. The main conclusions are as follows:

- (1) AFM analysis indicated that the f-GO showed a larger thickness, which was attributed to the presence of functionalized silane chains grafted on the graphene sheets. Zeta potential study well demonstrated that the dispersion of f-GO is better than that of GO.
- (2) The addition of GO and f-GO resulted in the increase of permeability and rejection. When the dosages were 1.0 wt%, the values of flux reached to the maximum and the lowest contact angle can be obtained.
- (3) An AFM analysis with a BSA-immobilized tip measured the weakest adhesion force with PVDF/f-GO membranes, while the nascent PVDF membranes and PVDF/GO membranes exhibited strong adhesion to the probe, consistent with the fouling properties of membranes.
- (4) After a ternary cycle BSA solution inner fouling process, the FRR was the highest for the P/f-GO membranes, indicating an impressive prospect for the antifouling performance and the recycle of the membranes.
- (5) Owing to the better interfacial interaction between f-GO sheets and PVDF matrix, the tensile strength and elongation-at-break of P/f-GO membranes show the best among the membranes.

In view of the conclusion discussed above, the superior performance of functionalized hybrid ultrafiltration membranes offers a great potential for practical application. Further studies will continue to explore the capabilities of functionalized GO on the alleviative fouling behavior and enhanced mechanical strength.

#### Acknowledgments

The work was funded by the National Natural Science Foundation of China (11175130, U1362108), the China Postdoctoral Science Foundation (2012M520578) and the Jiangsu Planned Projects for Postdoctoral Research Funds (1202067C).

#### Appendix A. Supporting information

Supplementary data associated with this article can be found in the online version at <http://dx.doi.org/10.1016/j.memsci.2014.01.050>.

#### Nomenclature

$A$	effective area of membranes ( $\text{m}^2$ )
AFM	atomic force microscope
APTS	3-aminopropyltriethoxysilane
BSA	bovine serum albumin
CA	contact angle (deg)
$C_F$	concentrations of BSA in the feed solution
$C_P$	concentrations of BSA in the permeation solution
DCC	$N,N'$ -dicyclohexyl-carbodiimide
DMAC	$N,N$ -dimethylacetamide
DMF	dimethyl formamide
$d_w$	water density ( $0.998 \text{ g cm}^{-3}$ )
f-GO	APTS-functionalized GO
FRR	flux recovery ratio
FTIR	Fourier-transform infrared spectroscopy
GO	graphene oxide
$J$	permeation flux of membrane for pure water ( $\text{L m}^{-2} \text{ h}^{-1}$ )
$J_{irr}$	pure water flux after cleaning membranes ( $\text{L m}^{-2} \text{ h}^{-1}$ )
$J_{mem}$	pure water flux through a clean membrane ( $\text{L m}^{-2} \text{ h}^{-1}$ )
$J_{pore}$	pure water flux after BSA permeation ( $\text{L m}^{-2} \text{ h}^{-1}$ )
$J_{tot}$	permeate flux of BSA after pure water flux ( $\text{L m}^{-2} \text{ h}^{-1}$ )
$J_{W1}$ (or $J_{W2}$ )	pure water flux of fouled membrane after being cleaned ( $\text{L m}^{-2} \text{ h}^{-1}$ )
$l$	membrane thickness (m)
PBS	phosphate buffer solution
PVDF	polyvinylidene fluoride
PVP	polyvinyl pyrrolidone
$Q$	volume of the permeate pure water ( $\text{m}^3 \text{ s}^{-1}$ )
$R$	rejection to BSA
$R_a$	adsorption resistance
$R_a$	mean roughness (nm)
$R_c$	concentration polarization resistance
$R_g$	cake layer resistance
$R_{ir}$	irreversible flux decline ratio
$R_m$	hydraulic resistance
$r_m$	membrane mean pore radius (nm)
$R_r$	reversible flux decline ratio
$R_t$	total flux decline ratio
$R_{tot}$	total filtration resistance
$T$	permeation time (h)
TMP	transmembrane pressure (MPa)
XPS	X-ray photoelectron spectroscopy
$\mu$	water viscosity (Pa s)

## References

- [1] S. Rajabzadeh, T. Maruyama, Y. Ohmukai, T. Sotani, H. Matsuyama, Preparation of PVDF/PMMA blend hollow fiber membrane via thermally induced phase separation (TIPS) method, *Sep. Purif. Technol.* 66 (2009) 76–83.
- [2] J. Jiang, L. Zhu, L. Zhu, B. Zhu, Y. Xu, Surface characteristics of a self-polymerized dopamine coating deposited on hydrophobic polymer films, *Langmuir* 27 (2011) 14180–14187.
- [3] J.R. Du, S. Peldszus, P.M. Huck, X. Feng, Modification of poly(vinylidene fluoride) ultrafiltration membranes with poly(vinyl alcohol) for fouling control in drinking water treatment, *Water Res.* 43 (2009) 4559–4568.
- [4] S. Zhao, Z. Wang, X. Wei, B. Zhao, J. Wang, S. Yang, S. Wang, Performance improvement of polysulfone ultrafiltration membrane using well-dispersed polyaniline-poly(vinylpyrrolidone) nanocomposite as the additive, *Ind. Eng. Chem. Res.* 51 (2012) 4661–4672.
- [5] A.K. Singh, P. Singh, S. Mishra, V.K. Shahi, Anti-biofouling organic-inorganic hybrid membrane for water treatment, *J. Mater. Chem.* 22 (2012) 1834–1844.
- [6] S. Majeed, D. Fierro, K. Bühr, J. Wind, B. Du, A. Boschetti-de-Fierro, V. Abetz, Multi-walled carbon nanotubes (MWCNTs) mixed polyacrylonitrile (PAN) ultrafiltration membranes, *J. Membr. Sci.* 403–404 (2012) 101–109.
- [7] Y. Sui, Z.N. Wang, X.L. Gao, C.-J. Gao, Antifouling PVDF ultrafiltration membranes incorporating PVDF-g-PHEMA additive via atom transfer radical graft polymerizations, *J. Membr. Sci.* 413 (2012) 38–47.
- [8] Q.-F. An, W.-D. Sun, Q. Zhao, Y.-L. Ji, C.-J. Gao, Study on a novel nanofiltration membrane prepared by interfacial polymerization with zwitterionic amine monomers, *J. Membr. Sci.* 431 (2013) 171–179.
- [9] Y. Chang, Y.-J. Shih, C.-Y. Ko, J.-F. Jhong, Y.-L. Liu, T.-C. Wei, Hemocompatibility of poly(vinylidene fluoride) membrane grafted with network-like and brush-like antifouling layer controlled via plasma-induced surface PEGylation, *Langmuir* 27 (2011) 5445–5455.
- [10] Z. Wang, H. Yu, J. Xia, F. Zhang, F. Li, Y. Xia, Y. Li, Novel GO-blended PVDF ultrafiltration membranes, *Desalination* 299 (2012) 50–54.
- [11] J. Lee, H.-R. Chae, Y.J. Won, K. Lee, C.-H. Lee, H.H. Lee, I.-C. Kim, J.-M. Lee, Graphene oxide nanoplatelets composite membrane with hydrophilic and antifouling properties for wastewater treatment, *J. Membr. Sci.* 448 (2013) 223–230.
- [12] Y. Zhao, Z. Xu, M. Shan, C. Min, B. Zhou, Y. Li, B. Li, L. Liu, X. Qian, Effect of graphite oxide and multi-walled carbon nanotubes on the microstructure and performance of PVDF membranes, *Sep. Purif. Technol.* 103 (2013) 78–83.
- [13] J. Zhang, Z. Xu, W. Mai, C. Min, B. Zhou, M. Shan, Y. Li, C. Yang, Z. Wang, X. Qian, Improved hydrophilicity, permeability, antifouling and mechanical performance of PVDF composite ultrafiltration membranes tailored by oxidized low-dimensional carbon nanomaterials, *J. Mater. Chem. A* 1 (2013) 3101–3111.
- [14] S. Chatterjee, F. Nafezarefi, N.H. Tai, L. Schlagenhauf, F.A. Nueesch, B.T.T. Chu, Size and synergy effects of nanofiller hybrids including graphene nanoplatelets and carbon nanotubes in mechanical properties of epoxy composites, *Carbon* 50 (2012) 5380–5386.
- [15] S.-Y. Yang, W.-N. Lin, Y.-L. Huang, H.-W. Tien, J.-Y. Wang, C.-C.M. Ma, S.-M. Li, Y.-S. Wang, Synergetic effects of graphene platelets and carbon nanotubes on the mechanical and thermal properties of epoxy composites, *Carbon* 49 (2011) 793–803.
- [16] X. Wang, W. Xing, P. Zhang, L. Song, H. Yang, Y. Hu, Covalent functionalization of graphene with organosilane and its use as a reinforcement in epoxy composites, *Compos. Sci. Technol.* 72 (2012) 737–743.
- [17] H. Yang, F. Li, C. Shan, D. Han, Q. Zhang, L. Niu, A. Ivaska, Covalent functionalization of chemically converted graphene sheets via silane and its reinforcement, *J. Mater. Chem.* 19 (2009) 4632–4638.
- [18] M.-Y. Shen, C.-F. Kuan, H.-C. Kuan, C.-H. Chen, J.-H. Wang, M.-C. Yip, C.-L. Chiang, Preparation, characterization, thermal, and flame-retardant properties of green silicon-containing epoxy/functionalized graphene nanosheets composites, *J. Nanomater.* 2013 (2013) 1–10.
- [19] A.Y. Park, H. Kwon, A.J. Woo, S.J. Kim, Layered double hydroxide surface modified with (3-aminopropyl)triethoxysilane by covalent bonding, *Adv. Mater.* 17 (2005) 106–109.
- [20] D.C. Marcano, D.V. Kosynkin, J.M. Berlin, A. Sinitskii, Z. Sun, A. Slesarev, L.B. Alemany, W. Lu, J.M. Tour, Improved synthesis of graphene oxide, *ACS Nano* 4 (2010) 4806–4814.
- [21] F.M. Shi, Y.X. Ma, J. Ma, P.P. Wang, W.X. Sun, Preparation and characterization of PVDF/TiO<sub>2</sub> hybrid membranes with different dosage of nano-TiO<sub>2</sub>, *J. Membr. Sci.* 389 (2012) 522–531.
- [22] V. Vatanpour, S.S. Madaeni, R. Moradian, S. Zinadini, B. Astinchap, Novel antifouling nanofiltration polyethersulfone membrane fabricated from embedding TiO<sub>2</sub> coated multiwalled carbon nanotubes, *Sep. Purif. Technol.* 90 (2012) 69–82.
- [23] C. Agarwal, A.K. Pandey, S. Das, M.K. Sharma, D. Pattyn, P. Ares, A. Goswami, Neck-size distributions of through-pores in polymer membranes, *J. Membr. Sci.* 415 (2012) 608–615.
- [24] A. Jayalakshmi, S. Rajesh, D. Mohan, Fouling propensity and separation efficiency of epoxidated polyethersulfone incorporated cellulose acetate ultrafiltration membrane in the retention of proteins, *Appl. Surf. Sci.* 258 (2012) 9770–9781.
- [25] J.F. Lapointe, S.E. Gauthier, Y. Pouliot, C. Bouchard, Characterization of interactions between beta-lactoglobulin tryptic peptides and a nanofiltration membrane: impact on the surface membrane properties as determined by contact angle measurements, *J. Membr. Sci.* 261 (2005) 36–48.
- [26] C. Wang, Q. Li, H. Tang, D. Yan, W. Zhou, J. Xing, Y. Wan, Membrane fouling mechanism in ultrafiltration of succinic acid fermentation broth, *Bioresour. Technol.* 116 (2012) 366–371.
- [27] E.C. Cho, D.-H. Kim, K. Cho, Contact angles of oils on solid substrates in aqueous media: correlation with AFM data on protein adhesion, *Langmuir* 24 (2008) 9974–9978.
- [28] H. Kim, Y. Miura, C.W. Macosko, Graphene/polyurethane nanocomposites for improved gas barrier and electrical conductivity, *Chem. Mater.* 22 (2010) 3441–3450.
- [29] K.B. Male, E. Lam, J. Montes, J.H.T. Luong, Noninvasive cell-based impedance spectroscopy for real-time probing inhibitory effects of graphene derivatives, *ACS Appl. Mater. Interface* 4 (2012) 3643–3649.
- [30] S.S. Madaeni, S. Zinadini, V. Vatanpour, Convective flow adsorption of nickel ions in PVDF membrane embedded with multi-walled carbon nanotubes and PAA coating, *Sep. Purif. Technol.* 80 (2011) 155–162.
- [31] G.C.-R.A. Bottino, G. Capannellic, S. Munaria, The formation of microporous poly(vinylidene difluoride) membranes by phase separation, *J. Membr. Sci.* 57 (1991) 1–20.
- [32] S. Liang, K. Xiao, Y. Mo, X. Huang, A novel ZnO nanoparticle blended poly(vinylidene fluoride) membrane for anti-irreversible fouling, *J. Membr. Sci.* 394–395 (2012) 184–192.
- [33] G. Arthanareeswaran, T.K.S. Devi, M. Raajenthiren, Effect of silica particles on cellulose acetate blend ultrafiltration membranes: Part I, *Sep. Purif. Technol.* 64 (2008) 38–47.
- [34] V. Vatanpour, S.S. Madaeni, L. Rajabi, S. Zinadini, A.A. Derakhshan, Boehmite nanoparticles as a new nanofiller for preparation of antifouling mixed matrix membranes, *J. Membr. Sci.* 401 (2012) 132–143.
- [35] P. Wang, J. Ma, Z. Wang, F. Shi, Q. Liu, Enhanced separation performance of PVDF/PVP-g-MMT nanocomposite ultrafiltration membrane based on the NVP-grafted polymerization modification of montmorillonite (MMT), *Langmuir* 28 (2012) 4776–4786.
- [36] G. Arthanareeswaran, P. Thanikaivelan, Fabrication of cellulose acetate-zirconia hybrid membranes for ultrafiltration applications: performance, structure and fouling analysis, *Sep. Purif. Technol.* 74 (2010) 230–235.
- [37] F. Liu, M.R.M. Abed, K. Li, Preparation and characterization of poly(vinylidene fluoride) (PVDF) based ultrafiltration membranes using nano gamma-Al<sub>2</sub>O<sub>3</sub>, *J. Membr. Sci.* 366 (2011) 97–103.
- [38] J.-F. Li, Z.-L. Xu, H. Yang, L.-Y. Yu, M. Liu, Effect of TiO<sub>2</sub> nanoparticles on the surface morphology and performance of microporous PES membrane, *Appl. Surf. Sci.* 255 (2009) 4725–4732.
- [39] M.R.M. Abed, S.C. Kumbharkar, A.M. Groth, K. Li, Economical production of PVDF-g-POEM for use as a blend in preparation of PVDF based hydrophilic hollow fibre membranes, *Sep. Purif. Technol.* 106 (2013) 47–55.
- [40] Z. Wu, H. Chen, X. Liu, Y. Zhang, D. Li, H. Huang, Protein adsorption on poly(N-vinylpyrrolidone)-modified silicon surfaces prepared by surface-initiated atom transfer radical polymerization, *Langmuir* 25 (2009) 2900–2906.
- [41] J.-H. Choi, J. Jegal, W.-N. Kim, Fabrication and characterization of multi-walled carbon nanotubes/polymer blend membranes, *J. Membr. Sci.* 284 (2006) 406–415.
- [42] W.R. N., Resistance of solid surfaces to wetting by water, *Ind. Eng. Chem.* 28 (1936) 988–994.
- [43] E. Yuliwati, A.F. Ismail, T. Matsuura, M.A. Kassim, M.S. Abdullah, Effect of modified PVDF hollow fiber submerged ultrafiltration membrane for refinery wastewater treatment, *Desalination* 283 (2011) 214–220.
- [44] G. Zhang, S. Lu, L. Zhang, Q. Meng, C. Shen, J. Zhang, Novel polysulfone hybrid ultrafiltration membrane prepared with TiO<sub>2</sub>-g-HEMA and its antifouling characteristics, *J. Membr. Sci.* 436 (2013) 163–173.
- [45] P. Anadao, L.F. Sato, H. Wiebeck, E.R. Valenzuela-Diaz, Montmorillonite as a component of polysulfone nanocomposite membranes, *Appl. Clay Sci.* 48 (2010) 127–132.
- [46] L.Y. Ng, A.W. Mohammad, C.P. Leo, N. Hilal, Polymeric membranes incorporated with metal/metal oxide nanoparticles: a comprehensive review, *Desalination* 308 (2013) 15–33.
- [47] P. Qin, X. Hong, M.N. Karim, T. Shintani, J. Li, C. Chen, Preparation of poly(phthalazinone-ether-sulfone) sponge-like ultrafiltration membrane, *Langmuir* 29 (2013) 4167–4175.
- [48] F. Zhang, W. Zhang, Y. Yu, B. Deng, J. Li, J. Jin, Sol-gel preparation of PAA-g-PVDF/TiO<sub>2</sub> nanocomposite hollow fiber membranes with extremely high water flux and improved antifouling property, *J. Membr. Sci.* 432 (2013) 25–32.
- [49] Y.C. Chiag, Y. Chang, W.Y. Chen, R.C. Ruaan, Biofouling resistance of ultrafiltration membranes controlled by surface self-assembled coating with PEGylated copolymers, *Langmuir* 28 (2012) 1399–1407.
- [50] V. Vatanpour, S.S. Madaeni, A.R. Khataee, E. Salehi, S. Zinadini, H.A. Monfared, TiO<sub>2</sub> embedded mixed matrix PES nanocomposite membranes: influence of different sizes and types of nanoparticles on antifouling and performance, *Desalination* 292 (2012) 19–29.
- [51] J. Meng, L. Song, H. Xu, H. Kong, C. Wang, X. Guo, S. Xie, Effects of single-walled carbon nanotubes on the functions of plasma proteins and potentials in vascular prostheses, *Nanomedicine* 1 (2005) 136–142.
- [52] H.Y. Ng, T.W. Tan, S.L. Ong, Membrane fouling of submerged membrane bioreactors: impact of mean cell residence time and the contributing factors, *Environ. Sci. Technol.* 40 (2006) 2706–2713.
- [53] C. Lv, Y. Su, Y. Wang, X. Ma, Q. Sun, Z. Jiang, Enhanced permeation performance of cellulose acetate ultrafiltration membrane by incorporation of Pluronic F127, *J. Membr. Sci.* 294 (2007) 68–74.

- [54] T.H. Bae, T.M. Tak, Effect of TiO<sub>2</sub> nanoparticles on fouling mitigation of ultrafiltration membranes for activated sludge filtration, *J. Membr. Sci.* 249 (2005) 1–8.
- [55] L. Fernandez, M. Sanchez, F.J. Carmona, L. Palacio, J.I. Calvo, A. Hernandez, P. Pradanos, Analysis of the grafting process of PVP on a silicon surface by AFM and contact angle, *Langmuir* 27 (2011) 11636–11649.
- [56] Y. Mo, A. Tiraferri, N.Y. Yip, A. Adout, X. Huang, M. Elimelech, Improved antifouling properties of polyamide nanofiltration membranes by reducing the density of surface carboxyl groups, *Environ. Sci. Technol.* 46 (2012) 13253–13261.
- [57] A. Asatekin, S. Kang, M. Elimelech, A.M. Mayes, Anti-fouling ultrafiltration membranes containing polyacrylonitrile-graft-poly (ethylene oxide) comb copolymer additives, *J. Membr. Sci.* 298 (2007) 136–146.
- [58] X. Yang, B. Zhang, Z. Liu, B. Deng, M. Yu, L. Li, H. Jiang, J. Li, Preparation of the antifouling microfiltration membranes from poly(N,N-dimethylacrylamide) grafted poly(vinylidene fluoride) (PVDF) powder, *J. Mater. Chem.* 21 (2011) 11908–11915.
- [59] J. Korfhagen, A.C. Dias-Cabral, M.E. Thrash, Nonspecific effects of ion exchange and hydrophobic interaction adsorption processes, *Sep. Sci. Technol.* 45 (2010) 2039–2050.
- [60] M. Zhou, H. Liu, A. Venkiteswaran, J. Kilduff, D.G. Anderson, R. Langer, G. Belfort, High throughput discovery of new fouling-resistant surfaces, *J. Mater. Chem.* 21 (2011) 693–704.
- [61] Z. Zhong, D. Li, B. Zhang, W. Xing, Membrane surface roughness characterization and its influence on ultrafine particle adhesion, *Sep. Purif. Technol.* 90 (2012) 140–146.
- [62] J. Mansouri, S. Harrisson, V. Chen, Strategies for controlling biofouling in membrane filtration systems: challenges and opportunities, *J. Mater. Chem.* 20 (2010) 4567–4586.
- [63] E.M. Vrijenhoek, S. Hong, M. Elimelech, Influence of membrane surface properties on initial rate of colloidal fouling of reverse osmosis and nanofiltration membranes, *J. Membr. Sci.* 188 (2001) 115–128.
- [64] W.R. Bowen, T.A. Doneva, Atomic force microscopy studies of membranes: effect of surface roughness on double-layer interactions and particle adhesion, *J. Colloid Interface Sci.* 229 (2000) 544–549.
- [65] X.-L. Li, L.-P. Zhu, B.-K. Zhu, Y.-Y. Xu, High-flux and anti-fouling cellulose nanofiltration membranes prepared via phase inversion with ionic liquid as solvent, *Sep. Purif. Technol.* 83 (2011) 66–73.
- [66] M. Sun, Y. Su, C. Mu, Z. Jiang, Improved antifouling property of pes ultrafiltration membranes using additive of silica-pvp nanocomposite, *Ind. Eng. Chem. Res.* 49 (2010) 790–796.
- [67] S.B. Teli, S. Molina, E.G. Calvo, A.E. Lozano, J. de Abajo, Preparation, characterization and antifouling property of polyethersulfone-PANI/PMA ultrafiltration membranes, *Desalination* 299 (2012) 113–122.
- [68] Y.Q. Wang, T. Wang, Y.L. Su, F.B. Peng, H. Wu, Z.Y. Jiang, Remarkable reduction of irreversible fouling and improvement of the permeation properties of poly (ether sulfone) ultrafiltration membranes by blending with pluronic F127, *Langmuir* 21 (2005) 11856–11862.
- [69] J. Peng, Y. Su, Q. Shi, W. Chen, Z. Jiang, Protein fouling resistant membrane prepared by amphiphilic pegylated polyethersulfone, *Bioresour. Technol.* 102 (2011) 2289–2295.